Experimental Mechanics
https://doi.org/10.1007/s11340-021-00693-x

RESEARCH PAPER

In-Situ SEM High Strain Rate Testing of Large Diameter Micropillars Followed by TEM and EBSD Postmortem Analysis

Z. Lin[1] · D. J. Magagnosc[3] · J. Wen[4] · C.-S. Oh[5] · S.-M. Kim[6] · H. D. Espinosa[1,2]

Received: 25 September 2020 / Accepted: 19 January 2021

Abstract

Background Dislocation dynamic simulations are intended as a tool to understand and predict the mechanical behavior of metallic materials, but its prediction has never been directly verified by experiments due to differences in specimen strain rate and size.

Objective In this work, a comprehensive experimental framework is proposed to attempt direct comparison between experiments and discrete dislocation dynamics (DDD) modelling.

Methods By integrating high-throughput sample fabrication and a customized testing apparatus, the sample size and strain rate typically employed in DDD simulations are explored experimentally. Constitutive properties such as stress-strain response are measured, and microstructural information is obtained from transmission electron microscopy (TEM) imaging, electron backscatter diffraction (EBSD), and TEM-based orientation mapping.

Results Magnesium and copper were selected, as case studies, to demonstrate the newly developed experimental procedure. Measured stress-strain responses for Mg are consistent with those obtained with a miniaturized Hopkison bar experiments. By exploiting the validated workflow, the effect of strain rate on micropillar heterogeneous deformation and associated dislocation plasticity were revealed.

Conclusion The work establishes a methodology for the systematic study of not only metals but also other materials and structures at the microscale and high strain rates.

Keywords *In situ* SEM · Magnesium · Microcompression · Micropillar · Strain rate effect

Introduction

The deformation mechanism of metals has been an active research topic within the mechanics of materials community. This is in part because of the synthesis of novel alloys (e.g., high entropy alloys) and because of the lack of a unified theoretical framework accounting for all the different constitutive behaviors found in metals and their alloys. Such behaviors vary drastically with the complexity of the material systems, the external environments, and size and time scale in which deformation events occur. For example, size-effects on mechanical properties of metals are prevalent and widely observed, with the earliest study tracing back nearly 100 years [1]. The sources of size-effects can be from either internal length scales, such as grain size in polycrystalline metals, layer thickness of multilayer samples, or the external length scale, e.g., the physical geometry of a sample. As for the latter, while bulk materials (with sample size down to sub-millimeter) have been extensively studied,

✉ H. D. Espinosa
espinosa@northwestern.edu

1 Theoretical and Applied Mechanics, Northwestern University, 2145 Sheridan Road, Evanston, Illinois 60208, USA

2 Department of Mechanical Engineering, Northwestern University, 2145 Sheridan Road, Evanston, Illinois 60208, USA

3 Army Research Laboratory, U.S, Aberdeen Proving Ground, Aberdeen, Maryland 21005, USA

4 Argonne National Lab, 9700 S. Cass Avenue, Lemont, Illinois 60439, USA

5 Department of Mechanical System Engineering, Kumoh National Institute of Technology, Gumi, Gyeongbuk 39177, Republic of Korea

6 Department of Nano-mechanics, Korea Institute of Machinery and Materials, Daejeon 34103, Republic of Korea

Published online: 31 March 2021

research on micrometer-scale samples is scarcer, which is partially due to the time -consuming sample preparation techniques available at this scale. In this regard, whiskers [2, 3] and pillars [4, 5] have been the most-studied specimens.

Specimens with dimensions ranging from a few to several tens of micrometers, present significant advantages in elucidating deformation mechanisms of metals. Unlike their counterparts at nano- and sub-micrometer-scales, where strengths are mostly controlled by dislocation nucleation [6–8] or dislocation starvation [9, 10], micrometer-scale samples exhibit dislocation-mediated deformation mechanisms similar to their bulk counterparts. More importantly, micrometer-scale systems can be directly analyzed using Discrete Dislocation Dynamics (DDD), to provide mechanistic understanding of their behaviors, and their microstructures characterized using X-ray diffraction and electron microscopy. Such a combined experimental-computational approach provides a unique opportunity to obtain stress-strain behavior, associated defect structures, and comparison with DDD model predictions.

While these characteristics make micrometer-scale systems a good candidate for understanding the deformation mechanisms and their impact on mechanical properties of metals, there are challenges in terms of sample preparation, sample handling, and development of experimental setups applicable at such small scale. Furthermore, most of the experimental efforts hitherto have focused on the mechanical behaviors at low strain rates [11, 12] (below 1/s), with rare excursion into the extreme high strain rate regime ($7 \times 10^5/s$) [13]. For microscale sample, the intermediate strain rate, namely $10^0 - 10^3$/s, of relevance to a number of applications such as automobile collision and drop of electronic components, requires further study. Also, from a scientific exploration viewpoint, absence of data at intermediate strain rates limits the opportunity of performing testing and characterization with direct comparison to modeling. In fact, the quasi-static strain rate employed in microscale experiments is not attainable even with state-of-the-art DDD algorithm [14], which can only predict material behavior at strain rates of 100/s or higher. One experimental technique, the miniature Kolsky bar method, [13] manages to achieve such experimental condition but preservation of the sample for post-mortem characterization remains a challenge. Therefore, there is a need for an experimental method that can obtain stress-strain behavior at intermediate strain rates in microscale samples and at the same time enabling postmortem defect type and density analysis to correlate mechanism to average behavior.

Recently, a micromechanical testing system based on piezo-actuation and piezo-sensing has been developed for high frequency nanoindentation experiments [15]. The system, by the brand name of Alemnis, can be reconfigured for high strain rate *in situ* scanning electron microscopy (SEM) micro-compression experiments [16]. In contrast to macroscale experiments where high strain rates are generated through impact, here it is achieved by a combination of fast crosshead velocity and small specimen dimensions. A similar concept was previously reported [17]. In this paper, we present a methodology for optimal preparation of array of micropillars with a range of diameters (1-50 μm), *in-situ* SEM intermediate strain rate compression testing, and post-mortem characterization via electron backscattering diffraction (EBSD) and TEM. As a case study and to demonstrate the efficacy of the experimental protocols we choose magnesium and copper, since their bulk counterparts have been extensively studied and comparisons to extract information on the effect of size scale can be readily made.

High-Strain-Rate Micropillar Compression Test

The experimental procedure is schematically summarized in Fig. 1. Micropillar specimens with a diameter of 15 μm and an aspect ratio of 2 to 3 are first prepared by a two-step method described later. Then, *in situ* SEM intermediate-strain-rate compression tests are carried out using a modified miniaturized testing platform, which will elucidate the stress-strain response of the materials. The as-prepared and post-mortem samples are subjected to microstructural characterization, including TEM imaging, EBSD, and TEM-based orientation mapping. These techniques will reveal the emergence and/or evolution of defects such as dislocation and twinning during the dynamic loading. These results together will enable an understanding of mechanical properties of materials from a mechanistic perspective, and help reveal the interplay between microstructures and forces in the materials.

Sample Preparation

Since Uchic et. al [4] pioneered the methodology of using focus ion beam (FIB) to fabricate micrometer size metallic pillars by lathe milling, many researchers have employed it and developed variations, such as annular milling [18]. A comparison between the two milling schemes, in terms of working principle and ion beam effects, was reported by Hütsch and Lilleodden [19]. While both methods have their own merit, they both suffer from the prolonged fabrication process and the resulting low throughput. Furthermore, the time required per sample fabricated increases approximately to the third power of its linear dimension. For this reason, very few studies have attempted pillars with diameter above 10 μm, where those that do, analyze only a couple of samples, which is not statistically significant and therefore susceptible to stochastic variations.

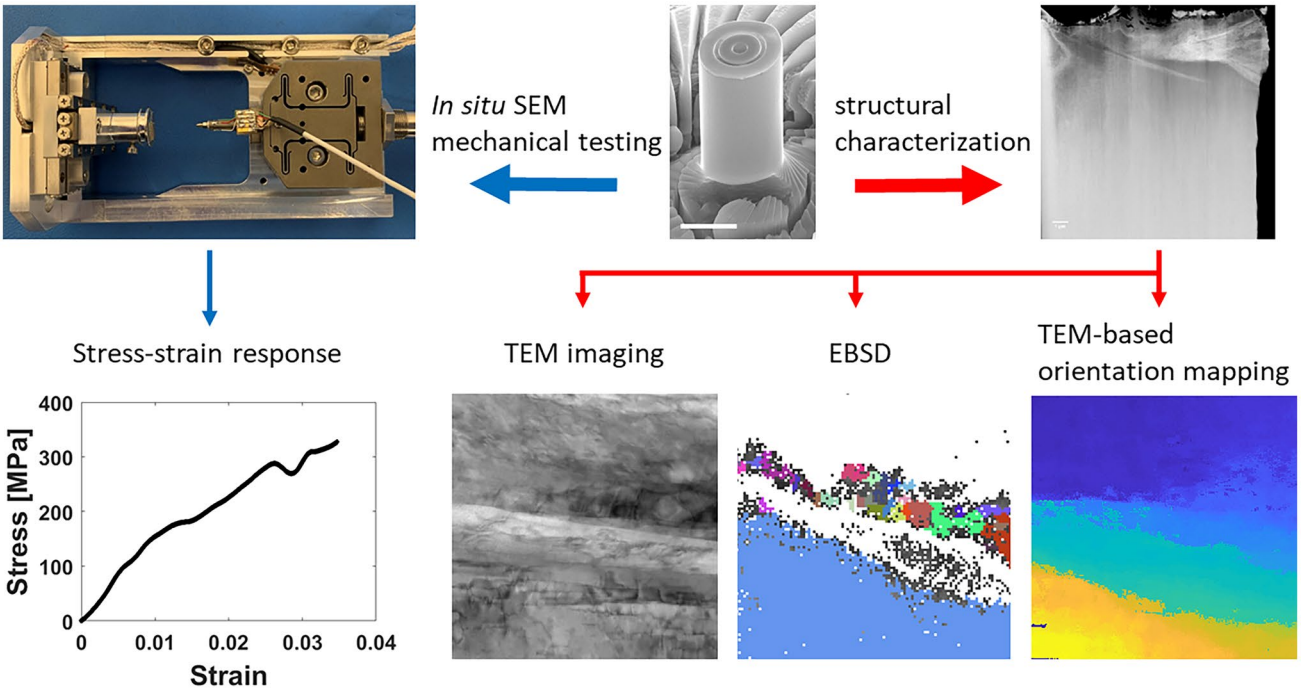

Fig. 1 The experimental procedure comprises mechanical characterization and microstructural characterization. The stress-strain response of the material is assessed by *in situ* SEM high-strain-rate testing, and the microstructural changes are characterized through techniques based on electron microscopy

Starting with bulk samples is the main reason for the low throughput achieved in the FIB-only fabrication method. FIB is a powerful instrument for making well-defined microstructures, but is not efficient in removing large volumes of material. In our approach, we start with less precise microfabrication methods to make arrays of pillars from a bulk piece of material; we then define the final pillar geometry by FIB removal of only a small outer layer followed by surface polishing. We demonstrate that femtosecond laser machining and chemical etching are two good candidates for the initial bulk material removal step.

An array of pillars was fabricated on single crystal <0001> Mg substrates, purchased from MTI Corporation. The substrate was processed by a femtosecond laser machining to generate pillars arranged in an array of ten rows by ten columns, with a 200-μm center-to-center distance between adjacent pillars, see Fig. 2. To achieve micropillars with final dimensions of 15 μm in diameter and a height of 30 μm, the coarse pillars were fabricated approximately twenty percent larger to leave enough material for precise final FIB milling and polishing. To enable some specialized sample characterization techniques, e.g., using X-rays, having pillars extending above substrate surface is required. This is also desirable for alignment between pillar and punch, as later discussed, for which observation in an edge-on manner without interference is helpful. Note that the two-step pillar fabrication method can achieve such pillar fabrication with ease, while removal of that much volume of material is practically impossible using solely FIB.

SEM images of the as-prepared laser-milled pillars are shown in Fig. 2(e)-(h). Through a parametric optimization of the laser machining, pillars with a smooth lateral surface and virtually debris-free tops were obtained. Figure 2(h) also shows a copper pillar prepared using a different set of laser parameters fine-tuned for this specific material. Due to re-deposition during the fabrication process, the top and the side of the pillars are covered with fine particulates of ablated material. It is likely that the laser-milling outcome is material dependent. Nevertheless, laser-milling proved to be a very fast way of preparing micro-scale samples, although additional precision for high throughput fabrication is needed in the case of Cu.

The effects of the femtosecond laser ablation on the microstructures of the targeted materials have been studied by M. Echlin et al [20]. It is shown that the depth of affected material is limited to a few micrometers for Cu. Since the depth of affected zone is related to the critical resolved shear stress in metals, similar phenomenon should be expected in Mg. Subsequent FIB milling will remove most of the induced dislocations and grains.

While the time required by laser milling is only a fraction of that with FIB milling (less than 5 minutes per micropillar),

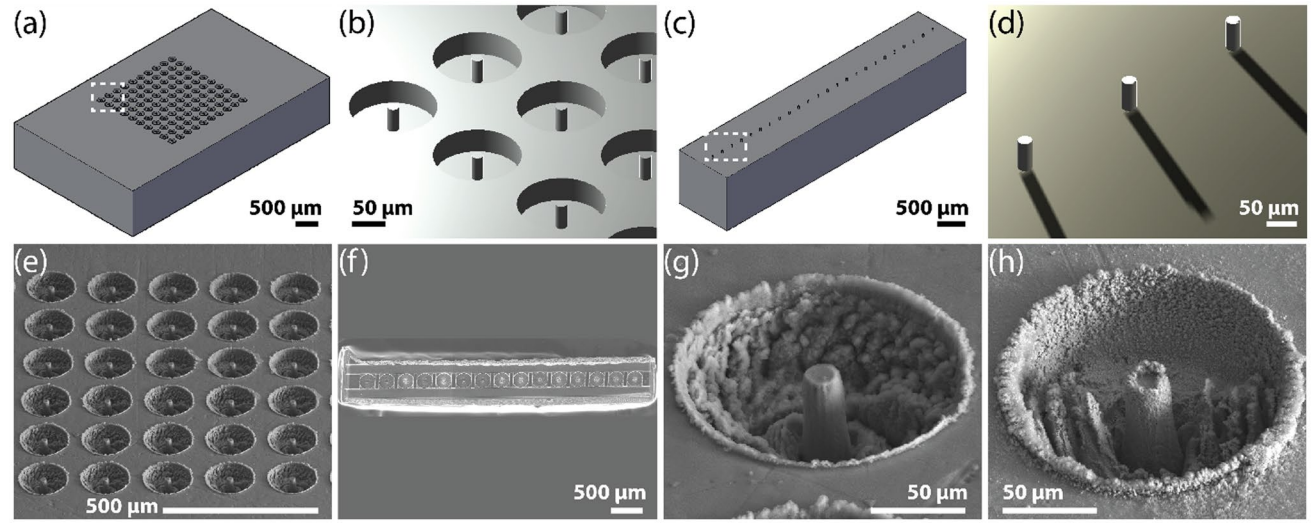

Fig. 2 Schematics of (**a**) an array of micropillars on a metallic substrates for mechanical compression tests, (**b**) close-up view of the region in (**a**) highlighted by dashed box, (**c**) an array of micropillars on a metallic substrates for X-ray characterization, and (**d**) close-up view of the region in (**c**) highlighted by dashed box. SEM images of (**e** and **f**) as-prepared Mg pillar arrays schematized in (**a** and **c**), (**g**) a Mg pillar, and (**h**) a Cu pillar

it still scales linearly with the volume to be removed. This is because the laser beam irradiates one spot at a time when the laser beam is scanned over the part surface. By contrast, chemical etching is a very efficient method for material removal over large patterned areas. Moreover, the time required by chemical etching is primarily dependent on the depth of the material to be removed, regardless of the etching area. The process requires fabrication of a mask defining the pattern of the pillars, typically achieved by photolithography, which is then transferred onto the substrate by etching. Since the method is applicable to isotropic and anisotropic material etching, it is suitable when dealing with single crystal metals upon selection of the right etchants. In the case of single crystal <100> Cu, ferric chloride was employed as etchant. For Mg, nitric acid was employed. As shown in Fig. 3, chemical etching results in pillars with exceptional surface flatness, which is critical in micro-compression experiments to avoid concentrated loading at asperities. The lateral surfaces defining the pillar walls, follow a typical isotropic etching curved surface.

The coarse pillars prepared by laser milling (Fig. 4(a)) or chemical etching, though possessing approximately the desired shape, required further milling with FIB to achieve the final dimensions and desired surface roughness. To minimize gallium implantation and potential embrittlement, FIB polishing currents were carefully selected and decreased gradually as the cutting pattern approached to final pillar dimensions. As can be seen in Fig. 4(b), annular FIB milling of the coarse pillars results in pillars with well-defined geometry and dimensions. However, the pillars exhibit the so-called curtaining effect, which manifests itself in the vertical lines observed on the side wall of a pillar. While this is inherent to the annular milling method, the roughness on the top surface aggravates this effect. Other undesirable features often associated with annular milling include a poorly defined height and a tapering shape of the pillar, the latter of which could significantly compromise the precision of a micro-compression test [21]. Therefore, this method should be reserved for the case where gallium implantation is a major concern.

Unlike annular milling where the ion beam is perpendicular to the sample surface, lathe milling removes material from the column's sidewalls with the ion beam at 52° with respect to the pillar's axis. During the milling process, a series of stage motions and rotations is performed facilitated by image correlation. While this scheme yields high accuracy in geometry and high surface smoothness, it inevitably increases the exposure to gallium ion of the pillar. Nevertheless, in the case of pillars with diameter of 15 µm, the effect of ion implantation on the mechanical behaviors is anticipated to be negligible. Using the algorithm developed by Uchic and Dimiduk [22], the coarse pillars prepared by laser milling or chemical etching can be readily refined to produce final pillars with the desired dimensions, as shown in Fig. 4(c).

Dynamic Behavior of the Apparatus and Its Calibration

The micromechanical testing apparatus used in our experiments, the Alemnis indenter, consists of several components. The rightmost component, a piezoelectric

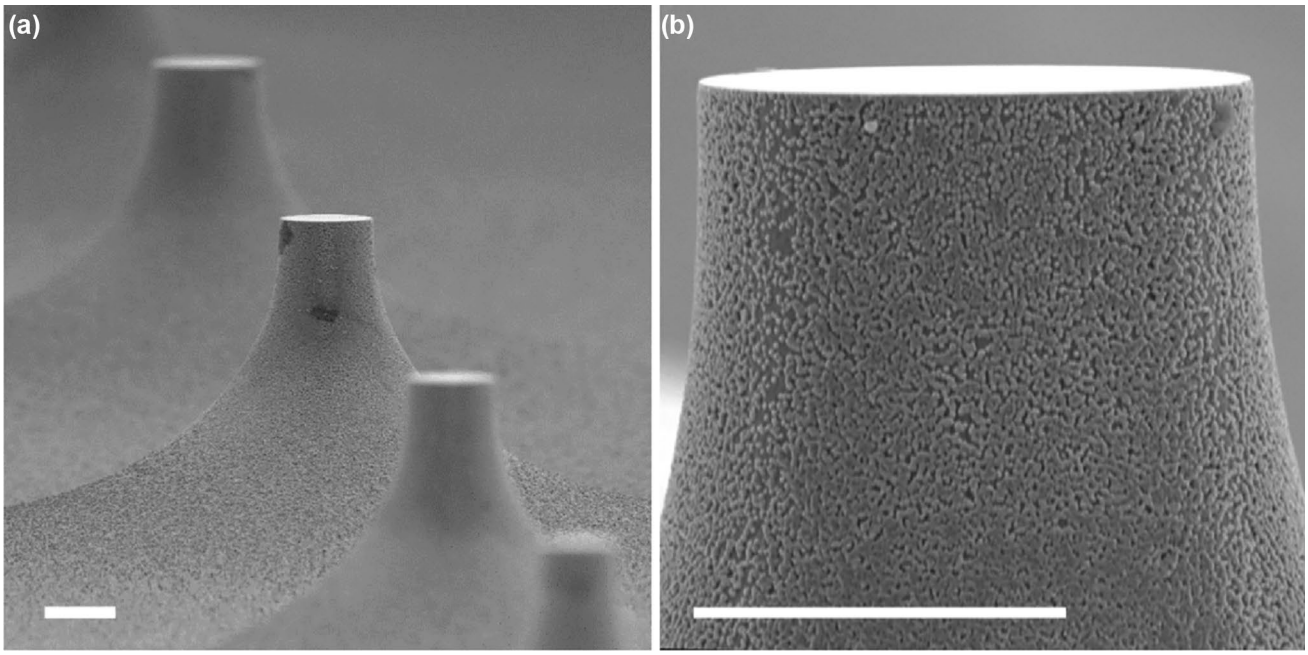

Fig. 3 (**a**) Coarse Cu pillar array fabricated by chemical etching. (**b**) Smooth top surface of the pillar as opposed to rough one caused by laser milling. Scale bar: 10 μm

actuator, is subjected to a predetermined voltage profile (waveform) to generate displacements at very high speeds. This displacement induces motion of a spring-like structure (strain gage), which in turn induces high-speed motion of a piezoelectric sensor mounted to the strain gage and a diamond flat punch. Figure 5(a) shows a top view of the Alemnis indenter configured in dynamic mode.

While the displacement of the diamond flat punch is measured by the strain gage, the force exerted on the diamond flat punch is measured by the piezoelectric sensor. When strained, the piezoelectric sensor accumulates charge, which is amplified and converted to a voltage signal. On the left side, the substrate containing the micropillars is glued to an SEM stub and mounted to a stage that moves along two orthogonal directions (X-Y) perpendicular to the axial compression direction (Z).

Displacement of the punch and the force exerted on the punch are the only two quantities measured during experiments. With the data acquisition electronics provided with the Alemnis indenter, we are able to measure displacement at a sampling rate of 50 kHz, and force at 220 kHz. We started by running a calibration test without a sample at high speed to assess how well the specified displacement profile was followed by the system, and to obtain a baseline force signal.

The results of the calibration tests are summarized in Fig. 5(b)-(d). A prescribed voltage profile, as shown in Fig. 5(b), was applied to the piezoelectric actuator. The induced actuator displacement was measured as shown in Fig. 5(c). As the voltage is ramped from 0 V to 20 V, the displacement linearly increases to 3.3 μm in 0.5 ms, equivalent to a speed of 6.6 mm/s.

While in calibration mode, the punch is not compressing anything; hence, one would expect the force measured by the piezoelectric sensor to be around 0 mN. However, we observe a nonzero "force signal" from the sensor, as plotted in Fig. 5(d). The reason for the existence of non-zero force is related to the inertia of the components as characterized below. Moreover, observation of the time dependent displacement and force signals, reveals that the sampling rate provided by the Alemnis data acquisition electronics is not sufficient. To overcome such limitation, we used an oscilloscope with GHz sample capability to increase the fidelity of the measured force time history.

To further characterize the baseline force signal induced by actuation of the actuator, in the absence of a specimen, 4 dry runs were performed at three ramp rates, namely, 40 kV/s, 200 kV/s and 400 kV/s. The peak voltage was kept constant at 20 V. The measured force signals are summarized in Fig. 6.

For any given ramp rate, signals from different runs are highly repeatable. Signals from different ramp rates, regardless of their difference in amplitude, have very similar time scales. These two features suggest that the nonzero force signal is not electrical cross talk. Therefore, before micropillar testing, the baseline was obtained and later subtracted from the measurements performed on micropillar samples.

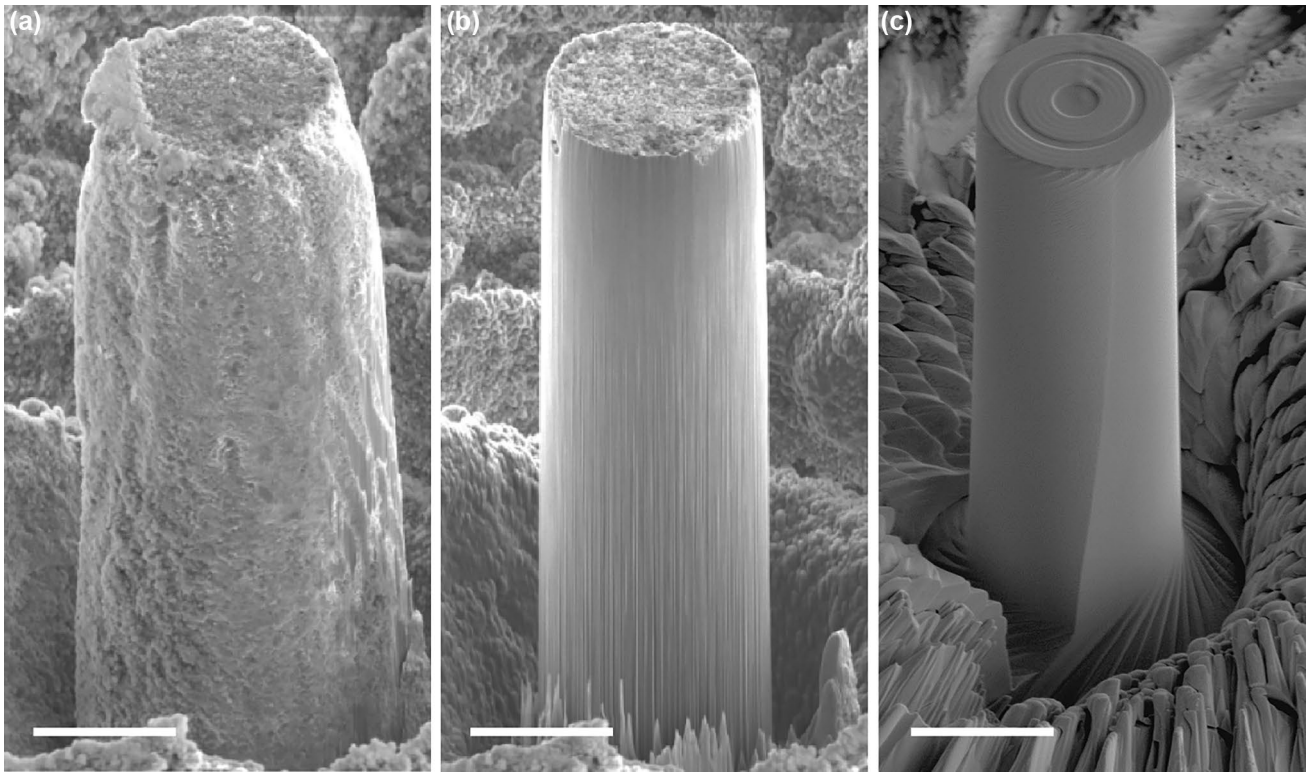

Fig. 4 (**a**) SEM image of a magnesium pillar as prepared by laser-milling and (**b**) after 2-hour FIB polishing. (**c**) A fine copper pillar prepared by lathe milling. Scale bar: 10 μm

To unveil the source of the force baseline and confirm the suitability of the background load subtraction, we performed a dynamic analysis of a lumped system consisting of spring, masses and dampers to capture elastic, inertia, and dissipative processes. The modeled system and parameters are shown in Fig. 7. The symbols, their definition and

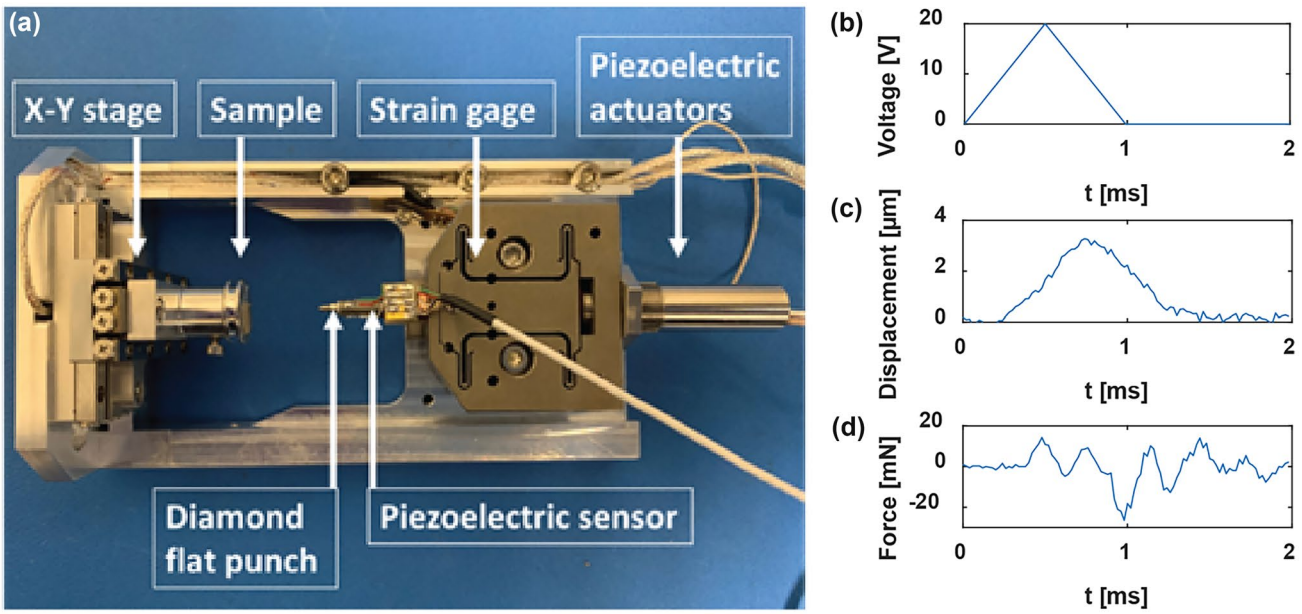

Fig. 5 (**a**) Photograph of Alemnis indenter configured in dynamics mode. (**b**) Voltage profile which is applied to the piezoelectric actuator. (**c**) Displacement history of the punch. (**d**) Force signal measured by the piezoelectric sensor

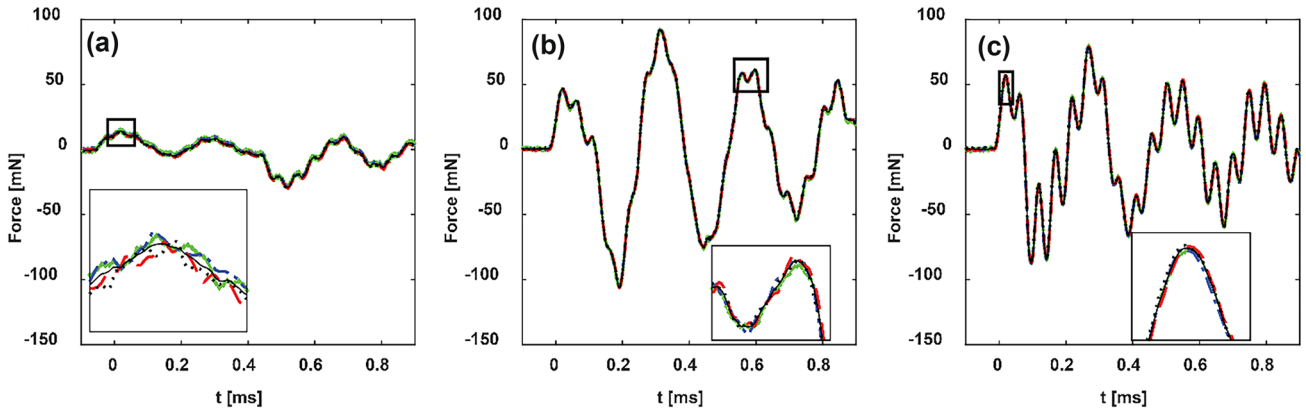

Fig. 6 Force signals without sample measured by piezoelectric sensor at ramp rate of (**a**) 40 kV/s, (**b**) 200 kV/s and (**c**) 400 kV/s. The insets highlight the fine-scale features and repeatability of the force signal

values are listed in Table 1. The values of the parameters are estimated by considering the properties and dimensions of the respective parts. The stiffness of the pillar is estimated using data from our compression experiments. Due to the complexity of the loading system, some parameters cannot be directly obtained. Therefore, we selected them such that the simulation result are consistent with the background force measurements.

The governing equations for masses m_1 and m_2 are:

$$m_1\ddot{x}_1 + c_1\left(\dot{x}_1 - \dot{x}_0\right) + k_1\left(x_1 - x_0\right) + k_2\left(x_1 - x_2\right) = 0$$

and

$$m_2\ddot{x}_2 + c_2\left(\dot{x}_2 - \dot{x}_1\right) + k_2\left(x_2 - x_1\right) + F_s = 0,$$

respectively, where $x_{1(2)}$ is the displacement of the left (right) side of the load sensor. F_s is the compression force on the pillar. The initial conditions are $\dot{x}_1(0) = x_1(0) = \dot{x}_2(0) = x_2(0) = 0$.

We performed two extreme simulations to gain insight into the system response. The system is driven by a piezoelectric actuator delivering a constant velocity $v = \dot{x}_0$. There is a tiny initial gap between the punch and the pillar. After the punch impacts the pillar, the actuator moves by another 1.5 µm before reversing the direction of motion.

We examined two extreme cases. One with a perfectly plastic sample and another with a purely elastic sample. In both cases, $F_s = 0$ before the punch impacts the pillar. For the purely elastic case, $F_s = k_3\left(x_2 - x_{20}\right)$ after the punch and the pillar are in contact, where x_{20} is the displacement of the punch to contact the pillar, i.e., the magnitude of the initial gap. For the perfectly plastic case, $F_s = k_3\left(x_2 - x_{20}\right)$ applies when the punch is moving towards the right. When the punch retracts $F_s = 0$.

The results of the simulations are presented in Fig. 8. For the case of a pure plastic pillar (no spring-back) the displacement of the punch, x_2, and the prescribed displacement, x_0, show good agreement with each other Fig. 8(a). The force signal measured by the load sensor is calculated as $k_2\left(x_1 - x_2\right)$, Fig. 8(b), where the background signal is obtained by running the simulation with $k_3 = 0$. The result shows that, after the punch hits the pillar at around 0.08 ms, the signal deviates from the background signal. After the punch is retracted, the signal once again matches the background force. The difference between the measured signal and the background force is taken as the measurement of the compressive force in the pillar. Figure 8(c) plots the subtracted signal along with the theoretical compressive force given by $F_s = k_3\left(x_2 - x_{20}\right)$. The analysis clearly shows that the force sensed by the load sensor, less the background force, is indeed the force between the punch and the pillar. Figure 8(d)-(f) show the results for a purely elastic pillar. Background force subtraction once again provides the force acting on the pillar.

The validity of the model can be assessed by comparison to an experiment conducted on a Mg pillar with 15-µm diameter and 30-µm height, in which the actuator moves at a speed of around 3 mm/s. From examination of Fig. 9, it is clear that the lumped model is capable of capturing the frequency and magnitude of the background oscillation.

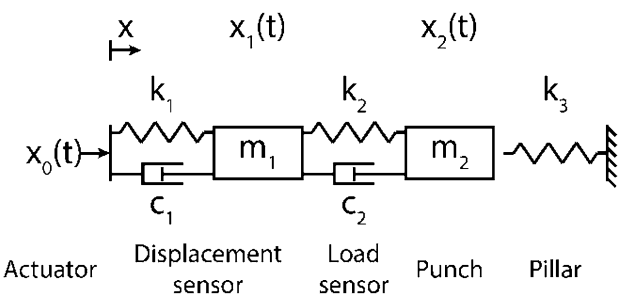

Fig. 7 Lumped model used for dynamic analysis of the system

Table 1 Parameters used in the lumped system

Symbol	Parameter	Value
$k_{1(2)}$	stiffness of the displacement sensor (load sensor)	10^7 N/m (10^8 N/m)
$m_{1(2)}$	mass of the displacement sensor (punch)	10 g (0.1 g)
$c_{1(2)}$	damping coefficients	100 N·s/m (200 N·s/m)
k_3	stiffness of the pillar	4×10^4N/m
$v = \dot{x}_0$	velocity of the piezoelectric actuator	±3 mm/s

Furthermore, the fact that the actual signal (red) converges to the background (blue), after the punch-sample contact vanishes, is further indication of the lumped model applicability. Hence, the protocol of obtaining the force on the specimen by subtracting the background can be applied with confidence. With increasing strain rate, the actuator dynamics leads to more vibration in the punch displacement, resulting in a more significant departure from the desired applied motion. In this regard, the model here introduced provides a useful tool to assess the suitability of the testing system for high-strain-rate experiments.

Limitation of the Alemnis Setup and Improvements

The original Alemnis tester is a ready-to-go commercial experimental setup that provides a quick and cost-effective solution, yet there are some compromises that require careful consideration in the context of high-strain-rate testing. The adoption of an oscilloscope with GHz sampling rate for load and displacement measurements is highly recommended. Besides the limitations in load measurement, the Alemnis tester electronics is unable to generate a voltage profile with the desired temporal resolution for high strain rate testing, and the maximum displacement sampling rate is 50 kHz, preventing accurate measurement of tip displacements essential to high strain rates experiments.

These shortcomings are overcome by two simple modifications. First, an arbitrary waveform generator with a sampling rate of 80 MHz, instead of the built-in waveform generator, was deployed to power the piezoelectric actuators. Second, before running an actual test with a sample in place, the same voltage profile is applied to the piezoelectric actuator several times and the displacement histories measured by the strain gage are recorded and averaged. Assuming the displacement of the tip is repeatable and not affected by the presence of the sample, a reasonable assumption for micropillars, the displacement measurement is fully characterized. For completeness, the displacement profiles are also measured during the tests with micropillar samples. The almost identical displacement profiles, obtained with and without samples, validates our assumptions.

The voltage applied to the piezoelectric actuator is initially held at 0 V. When the test starts, it increases to V/2 in the first quarter of the experiment with duration t. The subsequent two quarters see the voltage drop from V/2 to –V/2, which increases back to 0 V in the last quarter. Ideally, the displacement of the tip should follow the same

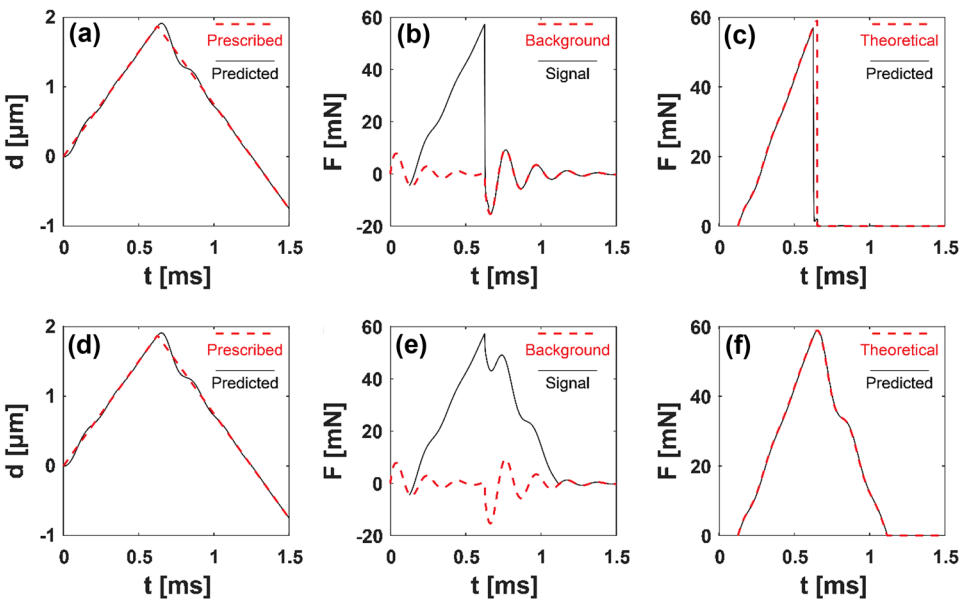

Fig. 8 Simulation results showing the dynamic response of the system. (**a**)-(**c**) are the results for the case of purely plastic pillar with no spring-back. (**a**) Comparison between prescribed actuator displacement and predicted displacement of the punch. (**b**) Background force and actual signal obtained without and with the pillar, respectively. (**c**) The theoretical force calculated as $F_s = k_3(x_2 - x_{20})$ and the predicted measurement taken as the difference between the signal and the background plotted in (**b**). Panels (**d**)-(**f**) correspond to the results for the case where the pillar is purely elastic

trend. However, as the voltage rate increases, the response of the actuator lags the theoretical response, and the speed at which the actuator moves is not proportional to the rate of the applied voltage. Two examples are shown in Fig. 10. While the voltage rate increases by a factor of 10 between Fig. 10(a) and (b), respectively, the speed of the actuator increases from ~3000 μm/s to 7200 μm/s, only a factor of 3 increase. Our characterization suggests that due to the inertia of the components in the current setup, further increase in the voltage will not significantly increase the speed of the actuator and the applicable sample strain rate. By comparing the average curves and the fitted lines, the uncertainty of displacement is estimated to be 53.8 nm and 76.3 nm for the cases given in Fig. 10(a) and (b), respectively.

Misalignment between the flat punch and the top surface of the micropillar can significantly affects the test accuracy by underestimating the elastic modulus, and may result in buckling of the pillar [21]. To minimize misalignment effects, the setup is enhanced with two tilting degrees of freedom through the addition of an optical mount (Newport™ M-P100-P), as shown in Fig. 11(a). It has been proposed to use maximum contact stiffness as an indicator for optimal alignment [23]. However, such indirect measurement of misalignment requires bringing the diamond flat and micropillar into contact. Here we follow a more direct misalignment correction procedure. Given the way that the setup is mounted on the SEM, as shown in Fig. 11(b), one can directly assess the alignment between the diamond punch and the sample mounted on the tilting platform, highlighted by green and red dash boxes, respectively. The process begins by first tilting the SEM stage such that the flat surface of the diamond punch appears edge-on, i.e., as a straight line in the SEM image. Then, by adjusting the two knobs on the sample mount, the top surface of the micropillar is made parallel to the flat punch surface, i.e., to appear edge-on as a parallel straight line. The accuracy of the procedure can be assessed by measuring the elastic modulus of single crystal Cu along the <100> direction.

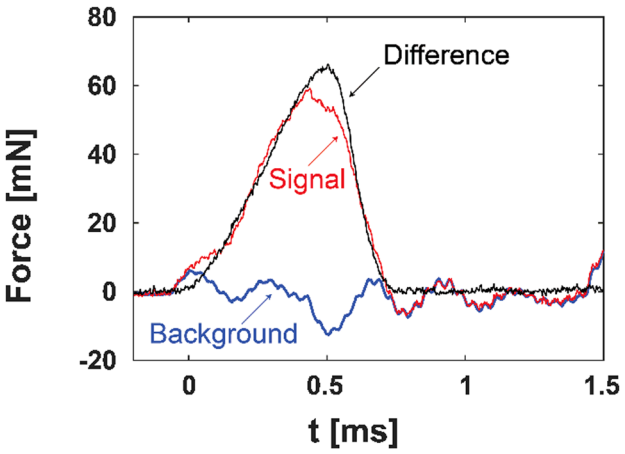

Fig. 9 Background signal without sample (blue curve), force signal with sample (red curve) and their difference (black curve), as obtained from a test of a 15 μm dia. pillar when the speed of the actuator was prescribed to 3 mm/s

Results

Stress-Strain Response at 85/s

A high strain-rate test was performed on a Mg pillar with diameter of 11.3 μm and height of 38 μm. Using the displacement

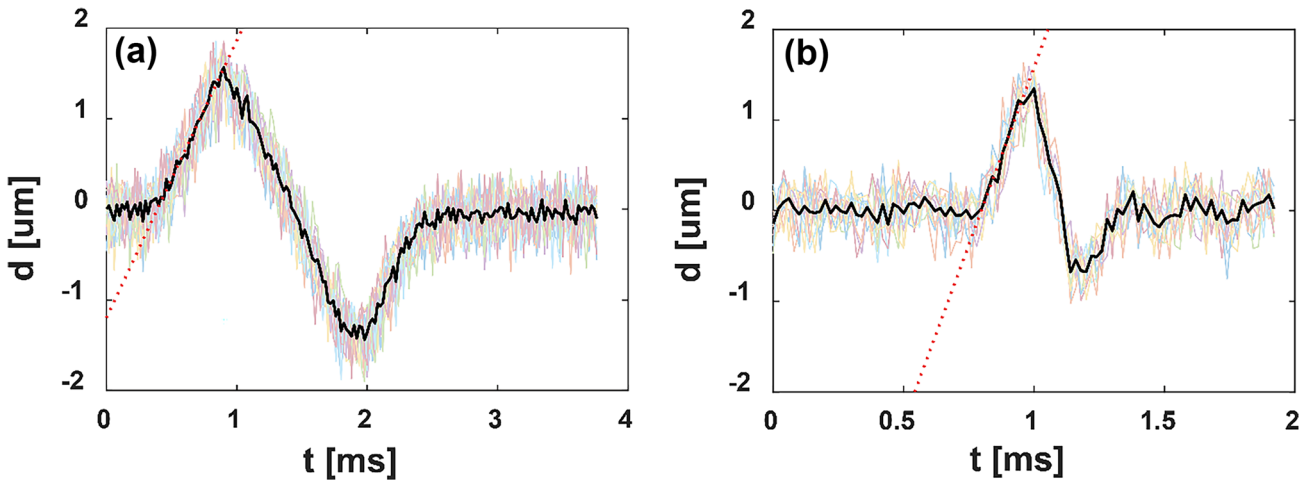

Fig. 10 Displacement profile of the piezo actuator in response to two different voltage profiles. (**a**) When subjected to V=1.06 V and t=2 ms, yielding a voltage rate (before amplification) of 1.06 V/ms, the actuator moves at 3059 μm/s. (**b**) When V=2.5 V and t=0.4 ms, the voltage rate is 12.5 V/ms and the actuator speed is 7204 μm/s. The thick black lines are the average of displacement profiles from at least 10 repeated tests in each case. The red dotted lines are fitted lines to the initial increasing portions of the averaged displacement profiles

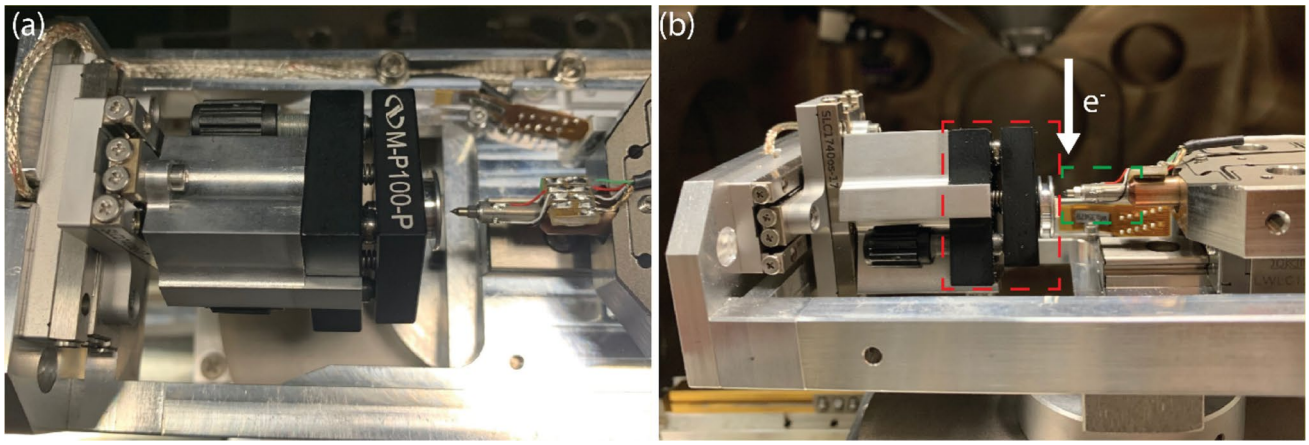

Fig. 11 (**a**) Top view of nanomechanical tester including tilt-correction platform. (**b**) Side view of tester as mounted in the SEM such that the gap between the top of the sample and the punch can be easily observed to achieve ideal alignment

profile presented in Fig. 10(a), a strain rate of around 85/s was imposed on the micropillar. Three force-time signals are reported in Fig. 12(a). The displacement history, not measured directly due to the low sampling rate of the built-in displacement sensor, is obtained from a calibration performed after a number of repeated measurements under the same actuation condition. As aforementioned, the force applied to the sample is obtained as the difference between the force measurement in the experiment with the pillar and the base line. The force and displacement profiles together yield the stress-strain curve of the sample, as shown in Fig. 12(b). The stress-strain curve for bulk Mg sample along the same crystalline direction loaded at 1200/s, reported in [24], is plotted alongside for comparison. The true strain ε_t and true stress σ_t in this work are obtained by assuming volume of the sample conserves and deformation happens uniformly, which gives $\varepsilon_t = \ln(1+\varepsilon)$ and $\sigma_t = \sigma(1+\varepsilon)$, where ε and σ are the engineering strain and stress, respectively.

Sample Preparation for Defect Identification and Characterization

A Mg micropillar tested at strain rate of 200/s was selected for TEM characterization. In the preparation of TEM sample by FIB milling, 15 kV was initially used to trim the pillar into a 5-μm-thick slab, which was further thinned to 2-μm at 10 kV, then 700-nm at 5 kV. Following the FIB process, the slab was subjected to ion milling at voltage of 2 kV for 20 minutes on both sides. The TEM sample slab within the pillar, and the crystallographic orientation of the TEM sample are schematically shown in Fig. 13(c). The foil plane is approximately $(2\ 11\ \bar{0})$.

TEM and EBSD Characterization

Mg pillars show concentrated deformation near the top of the pillar. Figure 13(a) and (b) show a micropillar before and after compression. The red dashed box in (b) highlights the region where TEM sample is extracted. TEM characterization was carried out in the FEI Talos F200X TEM/STEM at 200 kV. As reported in previous studies [25], the $\left\{11\ \bar{2}\ 2\right\}\langle 11\ \bar{2}\ 3\rangle$ is an active slip system for c-axis compression in Mg (Fig. 13(c)). Similar to what have been observed, dislocations in this slip system are strongly bound to the basal plane. Since the intersection of the slip plane and the sample foil plane lie on basal planes, it is expected to see high density of long dislocation segments in the TEM sample. Additional evidence

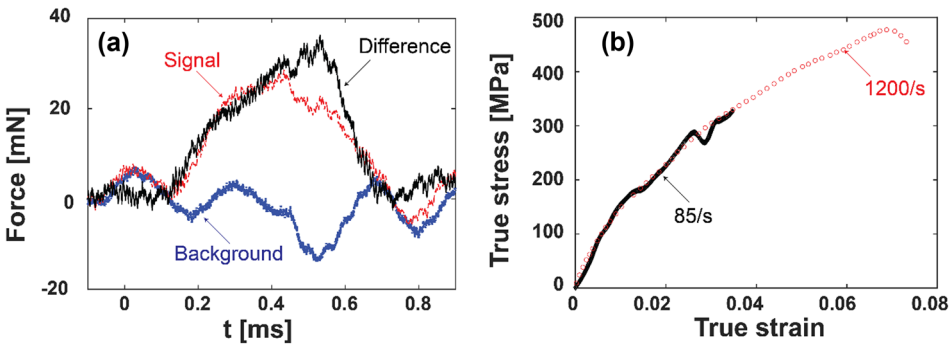

Fig. 12 (**a**) Background signal without sample (blue line), force signal with sample (red line) and their difference (black line). (**b**) Stress-strain response of Mg micropillars loaded at strain rates of 85/s and stress-strain curve for 1200/s for bulk samples, taken from [24]

of the activation of the $< \mathbf{a} + \mathbf{c} >$ dislocation under high strain rate is from TEM images taken under different diffraction conditions using the condition for invisibility, namely $\mathbf{g} \bullet \mathbf{b} = 0$, where **b** is the Burgers vector and **g** lattice plane selected for imaging. As shown in Fig. 13(d) and (e), dislocations are visible under (0001) reflection condition, but invisible under (01 $\bar{1}$ 0) reflection condition.

TEM images revealed that there are band-like structures extending several micrometers in the sample, which may be an indication of the presence of twinning or crystal rotation (Fig. 14). Therefore, it is of interest to perform EBSD on the sample to obtain a map of the crystalline orientation.

EBSD was carried out on the same sample for TEM analysis. Most of the area was mapped, but some small regions yielded no crystallographic orientation results, likely due to excessive lattice distortion. The pixel size used during mapping was set to 80 nm by 80 nm, with any grain smaller than this dimension not indexed. A detailed crystallographic picture is presented in Fig. 14(a), where the individual grains are shown by different colors, superimposed on its TEM image. Here a grain is defined as a misorientation greater than 1 degree. There are many small-angle boundaries near the band, while the bulk remains single crystal with little misorientation. Interestingly, the regions not indexed overlap with observed band in the TEM images. The EBSD result shows some spots in the crystal have undergone large rotation relative to the matrix.

Orientation Mapping for the Deformed Sample with Nanometer Size Electron Beam

EBSD provides plentiful information on grain structures, but its spatial resolution struggles in regions where large distortion of the crystal occur, such as the unindexed region on the EBSD map. An alternative is provided by a nano orientation mapping technique, which is carried out using the TOPSPIN system developed by NanoMEGAS, USA. It is a digital STEM, Beam Precession and Analytical Experimental Framework offering a suite of beam precession-enabled imaging and advanced analytical experiments. The orientation determination is based on nanobeam diffraction patterns, which is similar to the EBSD technique but with a much smaller bean size (down to 1 nm). The system is installed in a JEOL ARM 200F TEM, operated at 200 kV. Due to the limitations coming from the total acquisition time and the scanning area, the step size is set at 10 nm to achieve a balance between resolution and scanning area. The precession angle is 0.4 degrees. The acquisition time per diffraction pattern is only 0.01 s, enabling a scan covering a region of 2 μm by 2 μm with 40000 pixels to be finished in less than 7 minutes. Figure 14(b) shows the TEM image of the region, which is selected for nanobeam orientation mapping. Previously EBSD was used to map the orientation of a large area on the sample, but it was not capable of capturing details significantly smaller than the bean size. We are interested in the relative orientations of the crystal across the bend

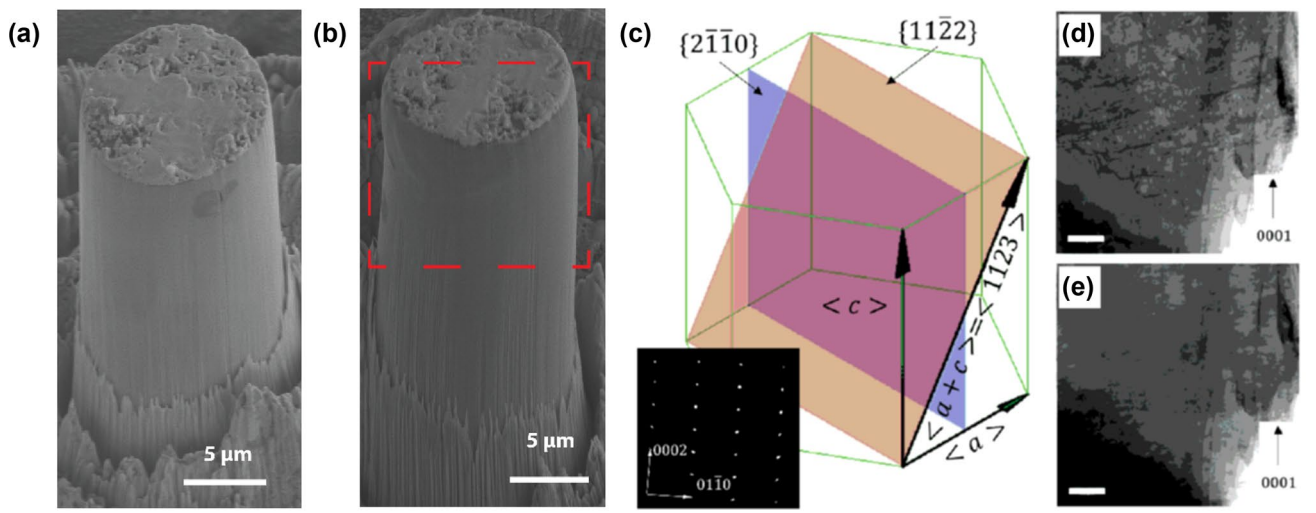

Fig. 13 A Mg pillar (**a**) before and (**b**) after compression. The red dash box in (**b**) highlights the place where the TEM sample is taken. (**c**) A schematic showing the hexagonal prism of the Mg crystal, the plane of the TEM sample which is $\{2\,11\,0\}$, and the $\{11\,\bar{2}\,2\}$ $<\bar{1}\bar{1}\,23>$ slip system. The inset shows the diffraction pattern taken at near the sample plane normal. The dislocations are visible for (**d**) 0001 reflection, but invisible for (**e**) 01 $\bar{1}$ 0 reflection. Scale bar: 200 nm

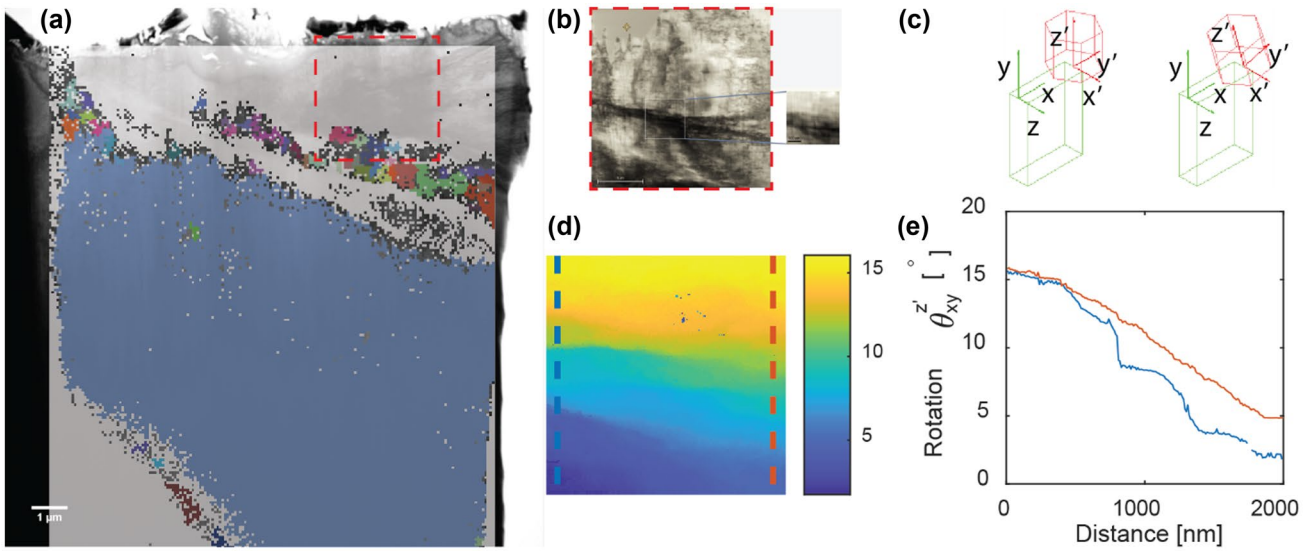

Fig. 14 (**a**) Grain distribution in the deformed pillar. Scale bar: 1 μm. (**b**) A region, highlighted in (**a**) where EBSD struggles to resolve crystallographic information, was selected for nano orientation mapping. (**c**) The sample reference frame (green) and the general crystal orientation (red). (**d**) $\theta_{xy}^{z'}$ at each pixel over the scan area. The deviation of the z' axis from the y axis varies from 2 degrees to 16 degrees. (**e**) The distribution of $\theta_{xy}^{z'}$ along two dashed lines in (**d**) are plotted as a function of distance (measured from top to bottom)

contour and the deduced microstructure type and critical dimensions.

Three Euler angles are used to describe the orientation of each pixel. The green coordinate system attached to the sample in Fig. 14(c) shows the sample reference frame, which is applied to each pixels in the sample. The x, y and z axes point leftward, upward and out-of-plane, respectively. The HCP unit cell is related to the sample by x-convention, in which the x-axis is aligned with the [2 11 0] direction in the crystal, schematically shown in the red coordinate system attached to the crystal in Fig. 14(c). The Euler angles are defined with respect to Bunge convention (zxz rotation).

It is valuable to use the general crystal orientation as a benchmark and compare it with the actual orientation of each pixel. For example, in the rotated frame attached to the crystal, the z' axis is approximately in alignment with the y axis of the sample reference frame, as shown in Fig. 14(b). An angle, $\theta_{xy}^{z'}$, which is defined as the angle between the projection of z' on the x-y plane and the y axis, can be used to describe by how much the z' axis deviates from its "standard" direction, which is along y axis in this case. If $\theta_{xy}^{z'} = 0$, z' axis is perfectly aligned with y axis at a given pixel. The value of $\theta_{xy}^{z'}$ at each pixel is plotted in Fig. 14(d). It can be clearly seen that the sample is divided into three regions, marked by different deviation angles of the z' axis. Figure 14(e) shows the deviation angle as a function of position along two dashed lines highlighted in Fig. 14(d). The blue curve shows a more discrete distribution of the rotation, marked by two steep jumps in rotation angle, while the red curve indicates that the rotation of the crystal along the red dashed line is more gradual.

Concluding Remarks

This paper presents an experimental approach for high strain rate mechanical testing and characterization on micrometer-scale specimens. From sample preparation to the *in situ* SEM testing module, the experimental procedure is standardized and can be readily applied to a wide range of materials, from solid to architected lattices, from crystalline to amorphous. Postmorten electron microscopy characterization of microstructure and defects, here reported using electron microscopy, proved to be a powerful tool for revealing deformation mechanisms and helped build a connection between mechanical behavior and underlying microstructural evolution.

As a part of this effort, several sample preparation methods, modifications to the measurement system, and experimental best practices were identified. Two complementary sample preparation techniques using either femtosecond laser machining or chemical etching were identified. These methods should facilitate higher throughput of specimens, essential to obtaining statistic insight, which is rare in micro- and nano-scale mechanical investigations. Requirements for the data acquisition electronics were identified, and the advantages of selecting high frequency signal generators and oscilloscopes demonstrated. Further efforts should be

dedicated to the improvement of displacement and load sensors in the mechanical setup, to extend the range of measurable strain rates. Finally, a method to correct for misalignment of the punch and micropillar was presented. The approach ensures a well-defined single axis loading and avoids unintended effects on the mechanical behavior or recorded signals, reducing data reduction complexity.

While this experimental procedure was applied to single crystal metals, its applicability to the study of many other material types, such as high entropy alloy and glasses is easily inferred. Indeed, they share common features in sample preparation, testing, and characterization techniques. Furthermore, the setup for high strain rate *in situ* SEM compression testing can be applied in the investigation of the dynamic behavior of metamaterials, such as lattices and origami-architected structures, at the microscale. So far, the mechanical behaviors of these structures was only probed at quasi-static strain rates, while their bulk counterparts are known to possess interesting properties at higher strain rates. Finally, the selected dimensions of the micropillars makes the samples amenable to more detailed post-mortem characterization. In the future, other characterization techniques, such as three-dimensional x-ray microscopy [26], will be explored when a non-destructive and three dimensional characterization is desirable.

Acknowledgements H. D. Espinosa gratefully acknowledge financial support from the Army Research Lab through award No. W911NF1220022. The authors thank Dr. Robert Stroud (NANOMEGAS USA) for acquiring the TEM nano-mapping data reported in Fig. 14(d) and acknowledge the Argonne National Lab - Center for Nanomaterial user awards 57577, 57549, and 67558.

Declaration

Conflict of Interests The authors declare that they have no conflict of interest.

References

1. Taylor GF (1924) A Method of Drawing Metallic Filaments and a Discussion of their Properties and Uses. Phys Rev 23:655–660. https://doi.org/10.1103/PhysRev.23.655
2. Brenner SS (1956a) The growth of whiskers by the reduction of metal salts. Acta Metall 4:62–74. https://doi.org/10.1016/0001-6160(56)90111-0
3. Brenner SS (1956b) Tensile strength of whiskers. J Appl Phys 27:1484–1491. https://doi.org/10.1063/1.1722294
4. Uchic MD, Dimiduk DM, Florando JN, Nix WD (2003) Exploring specimen size effects in plastic deformation of Ni 3(Al, Ta). Mater Res Soc Symp - Proc 753:27–32. https://doi.org/10.1557/proc-753-bb1.4
5. Uchic MD, Dimiduk DM, Florando JN, Nix WD (2004) Sample dimensions influence strength and crystal plasticity. Science (80-) 305:986–989. https://doi.org/10.1126/science.1098993
6. Bernal RA, Aghaei A, Lee S et al (2015) Intrinsic Bauschinger Effect and Recoverable Plasticity in Pentatwinned Silver Nanowires Tested in Tension. Nano Lett 15:139–146. https://doi.org/10.1021/nl503237t
7. Ramachandramoorthy R, Gao W, Bernal R, Espinosa H (2016) High Strain Rate Tensile Testing of Silver Nanowires: Rate-Dependent Brittle-to-Ductile Transition. Nano Lett 16:255–263. https://doi.org/10.1021/acs.nanolett.5b03630
8. Park HS, Cai W, Espinosa HD, Huang H (2009) Mechanics of Crystalline Nanowires. MRS Bull 34:178–183. https://doi.org/10.1557/mrs2009.49
9. Tang H, Schwarz KW, Espinosa HD (2008) Dislocation-Source Shutdown and the Plastic Behavior of Single-Crystal Micropillars. Phys Rev Lett 100:185503. https://doi.org/10.1103/PhysRevLett.100.185503
10. Zhu T, Li J, Ogata S, Yip S (2009) Mechanics of Ultra-Strength Materials. MRS Bull 34:167–172. https://doi.org/10.1557/mrs2009.47
11. Jennings AT, Li J, Greer JR (2011) Emergence of strain-rate sensitivity in Cu nanopillars: Transition from dislocation multiplication to dislocation nucleation. Acta Mater 59:5627–5637. https://doi.org/10.1016/j.actamat.2011.05.038
12. Jeong J, Alfreider M, Konetschnik R et al (2018) *In-situ* TEM observation of 10$\bar{1}$2 twin-dominated deformation of Mg pillars: Twinning mechanism, size effects and rate dependency. Acta Mater 158:407–421. https://doi.org/10.1016/j.actamat.2018.07.027
13. Casem D, Ligda J, Walter T et al (2020) Strain-Rate Sensitivity of Nanocrystalline Cu–10Ta to 700,000/s. J Dyn Behav Mater 6:24–33. https://doi.org/10.1007/s40870-019-00223-w
14. Sills RB, Bertin N, Aghaei A, Cai W (2018) Dislocation Networks and the Microstructural Origin of Strain Hardening. Phys Rev Lett 121:085501. https://doi.org/10.1103/PhysRevLett.121.085501
15. Guillonneau G, Mieszala M, Wehrs J et al (2018) Nanomechanical testing at high strain rates: New instrumentation for nanoindentation and microcompression. Mater Des 148:39–48. https://doi.org/10.1016/j.matdes.2018.03.050
16. Ramachandramoorthy R (2019) Deformation and Failure in Metallic Nanowires Under Stress-relaxation. Northwestern University, Cyclic and High Strain Rate Loading Conditions
17. Ben-David E, Tepper-Faran T, Rittel D, Shilo D (2014) A New Methodology for Uniaxial Tensile Testing of Free-Standing Thin Films at High Strain-Rates. Exp Mech 54:1687–1696. https://doi.org/10.1007/s11340-014-9911-1
18. Greer JR, Oliver WC, Nix WD (2005) Size dependence of mechanical properties of gold at the micron scale in the absence of strain gradients. Acta Mater 53:1821–1830. https://doi.org/10.1016/j.actamat.2004.12.031
19. Hütsch J, Lilleodden ET (2014) The influence of focused-ion beam preparation technique on microcompression investigations: Lathe vs. annular milling. Scr Mater 77:49–51. https://doi.org/10.1016/j.scriptamat.2014.01.016
20. Echlin MP, Titus MS, Straw M et al (2017) Materials response to glancing incidence femtosecond laser ablation. Acta Mater 124:37–46. https://doi.org/10.1016/j.actamat.2016.10.055
21. Zhang H, Schuster BE, Wei Q, Ramesh KT (2006) The design of accurate micro-compression experiments. Scr Mater 54:181–186. https://doi.org/10.1016/j.scriptamat.2005.06.043
22. Uchic MD, Dimiduk DM (2005) A methodology to investigate size scale effects in crystalline plasticity using uniaxial compression testing. Mater Sci Eng A 400–401:268–278. https://doi.org/10.1016/j.msea.2005.03.082

23. Zhao X, Strickland DJ, Derlet PM et al (2015) *In situ* measurements of a homogeneous to heterogeneous transition in the plastic response of ion-irradiated ⟨111⟩ Ni microspecimens. Acta Mater 88:121–135. https://doi.org/10.1016/j.actamat.2015.01.007
24. Li Q (2011) Dynamic mechanical response of magnesium single crystal under compression loading: Experiments, model, and simulations. J Appl Phys 109 https://doi.org/10.1063/1.3585870
25. Obara T, Yoshinga H, Morozumi S (1973) {11$\bar{2}$2} ⟨1123⟩ Slip system in magnesium. Acta Metall 21:845–853. https://doi.org/10.1016/0001-6160(73)90141-7
26. Larson BC, Yang W, Ice GE et al (2002) Three-dimensional X-ray structural microscopy with submicrometre resolution. Nature 415:887–890. https://doi.org/10.1038/415887a